Volume 24
Number 2
21 January 2024
Pages 153–386

Lab on a Chip

Devices and applications at the micro- and nanoscale

rsc.li/loc

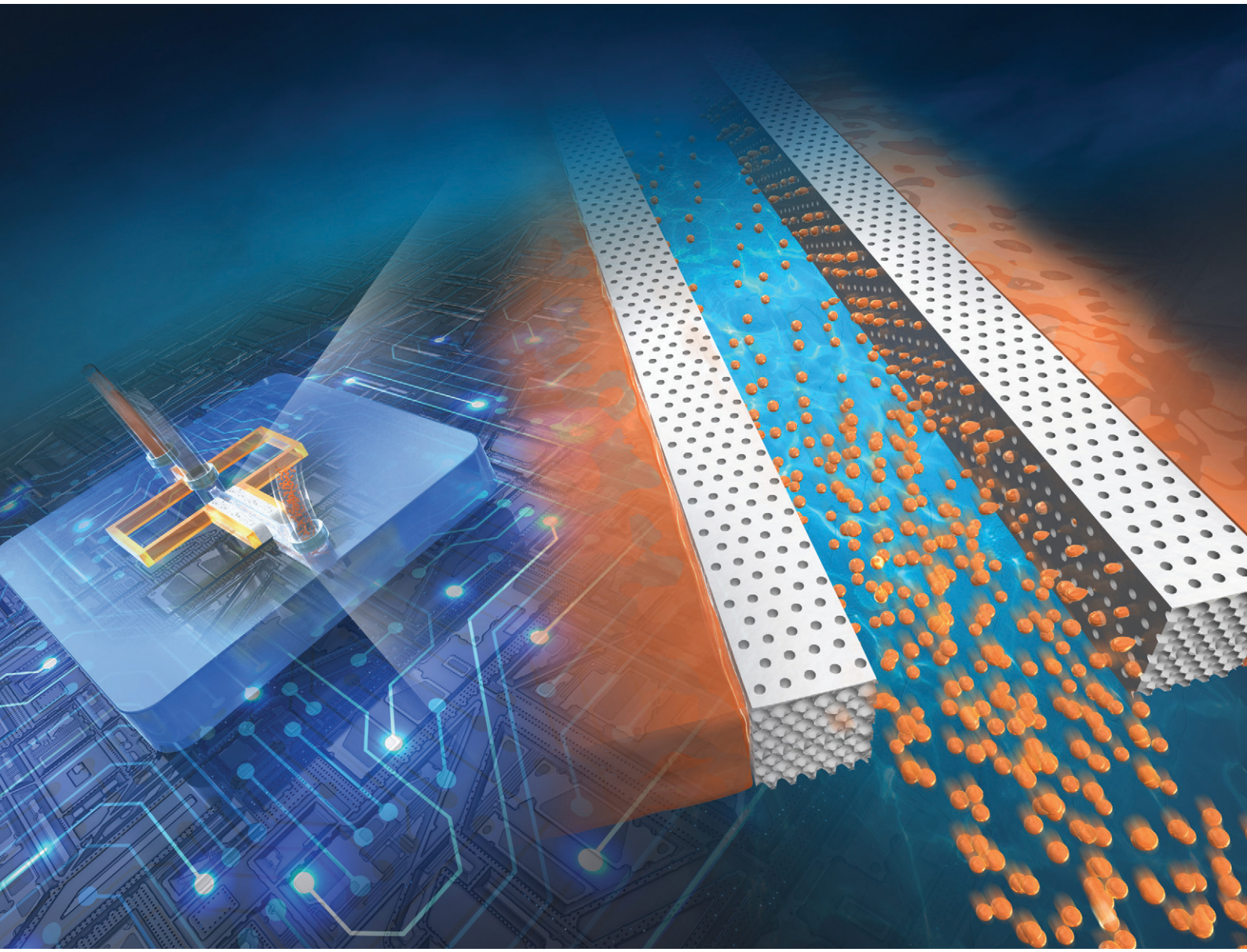

ISSN 1473-0197

ROYAL SOCIETY OF CHEMISTRY

PAPER

Masumi Yamada *et al.*

Pushing the limits of microfluidic droplet production efficiency: engineering microchannels with seamlessly implemented 3D inverse colloidal crystals

Lab on a Chip

PAPER

View Article Online
View Journal | View Issue

Cite this: *Lab Chip*, 2024, **24**, 171

Pushing the limits of microfluidic droplet production efficiency: engineering microchannels with seamlessly implemented 3D inverse colloidal crystals†

Shota Mashiyama, Runa Hemmi, Takeru Sato, Atsuya Kato, Tatsuo Taniguchi and Masumi Yamada *

Although droplet microfluidics has been studied for the past two decades, its applications are still limited due to the low productivity of microdroplets resulting from the low integration of planar microchannel structures. In this study, a microfluidic system implementing inverse colloidal crystals (ICCs), a spongious matrix with regularly and densely formed three-dimensional (3D) interconnected micropores, was developed to significantly increase the throughput of microdroplet generation. A new bottom-up microfabrication technique was developed to seamlessly integrate the ICCs into planar microchannels by accumulating non-crosslinked spherical PMMA microparticles as sacrificial porogens in a selective area of a mold and later dissolving them. We have demonstrated that the densely arranged micropores on the spongious ICC of the microchannel function as massively parallel micronozzles, enabling droplet formation on the order of >10 kHz. Droplet size could be adjusted by flow conditions, fluid properties, and micropore size, and biopolymer particles composed of polysaccharides and proteins were produced. By further parallelization of the unit structures, droplet formation on the order of >100 kHz was achieved. The presented approach is an upgrade of the existing droplet microfluidics concept, not only in terms of its high throughput, but also in terms of ease of fabrication and operation.

Received 24th October 2023,
Accepted 27th November 2023

DOI: 10.1039/d3lc00913k

rsc.li/loc

Introduction

Over the past two decades, micrometer-sized monodisperse droplets generated using microfluidic devices have created a variety of functionality and added value to droplet-based material production,[1,2] high-precision biochemical analysis,[3–5] and soft matter chemistry.[6–8] Numerous applications that were not feasible with conventional bulk-scale emulsification techniques have been realized with droplet microfluidics. In the processes of preparing particulate materials using droplets as templates, not only particle size but also morphology and anisotropy can be controlled.[9–12] Encapsulation of biomolecules, vesicles, and living cells also allows precise manipulation and digital analysis of target molecules in compartmentalized vessels.[13,14] In these studies, the advantages of droplet microfluidics, which dramatically increase droplet size controllability, are fully exploited.

In droplet generation techniques, the droplet size is determined by the balance of the interfacial tension and the shear force, under the influence of the fluid viscosity and the surface wettability of the apparatus.[15,16] In microfluidic channels, this balance is easily kept constant by continuously feeding the continuous and dispersed phases, resulting in the formation of monodisperse droplets. Typical structures for this purpose are the microchannel confluences, such as a T- or Y-shaped junctions[17–19] and flow-focusing structures.[20,21] Step emulsification with terrace structures of different depths[22,23] and co-flow channels with double tubes[24–26] have also been proposed. Despite their ability to control droplet size, droplet generation processes using a single microchannel confluence usually suffer from the critical limitation of low production throughput. The number-base droplet production speed depends on the type of droplet generation scheme (*e.g.*, squeezing, dripping, and jetting), but most droplet generation frequencies using a flow-focusing scheme or T-junction are on the order of several hundred Hz,[17,27–32] and only a limited number of systems are able to produce microdroplets at high

Department of Applied Chemistry and Biotechnology, Graduate School of Engineering, Chiba University, 1-33 Yayoi-cho, Inage-ku, Chiba 263-8522, Japan. E-mail: m-yamada@faculty.chiba-u.jp

† Electronic supplementary information (ESI) available: Movie S1 showing the generation behaviors of droplets in the device. See DOI: https://doi.org/10.1039/d3lc00913k

frequency.[33] Consequently, applications for particulate preparation that use droplets as templates require long-term operations to ensure sufficient productivity. However, such operations may cause problems, including clogging of microchannels and time-dependent instability of droplet generation.

One of the most intuitive strategies for increasing the droplet production throughput is to employ parallelized microchannels.[34,35] In a pioneering study by Nisisako *et al.*, droplet-forming channels were arranged in a circular pattern and vertically stacked, thereby forming $\sim 1 \times 10^5$ droplets per second.[36] Branched microchannel networks have also been employed to increase the number of the T-junctions.[37–39] Step emulsification-based parallel productions of small droplets using long terrace-like channels have also been reported.[40–42] Most of these approaches parallelized droplet-forming junctions in a linear assembly, resulting in one to two orders of magnitude more droplet formation compared to a single channel structure. However, the microchannel networks for these studies were formed on a 2D plane, and there is a limitation in the degree of integration/parallelization of the planar microchannels prepared with conventional photolithography or micromachining. Stacking of multiple plates has been demonstrated, but the complexity in creating 3D channel networks has the potential to compromise the operability and credibility of the experiments. Arrangement of numerous droplet-forming structures on a 2D plane would be an alternative strategy,[43] but the device fabrication process, especially the creation of through holes on a thin wafer by dry etching or laser machining, would be significantly costly.

Recently, novel approaches for the creation of functional 3D micro/nanostructures using bottom-up processes have been intensively studied.[44] In particular, various methods to engineer PDMS with microporous structures have been developed. For instance, PDMS-based porous microneedles as a biosensor for continuous monitoring have been proposed.[45] Cell culture devices integrated with porous PDMS sponges have also been reported,[46] in which the direct medium supply to the cells improved cell functions and viability. Fabrication of such 3D structures using polydimethylsiloxane (PDMS) as the material would facilitate the integration and incorporation of the structures into PDMS-based microfluidic devices. In fabricating these porous substrates, various types of porogens, including solid particles,[45–48] water bubbles[49] and ice particles,[50] have been utilized as sacrificial sources for the creation of pores. Among them, the use of uniformly sized spherical particles as the porogen facilitates the formation of so-called inverse colloidal crystals (ICC) or inverse opals, in which the surface/internal pores are uniformly and densely arranged.[51–53] We expected that the surface micropores of such ICCs could be used as micronozzles for droplet formation to enable high-throughput droplet formation. However, to the best of our knowledge, no such studies have been reported, possibly because of the difficulty in establishing a mechanism that can deliver the continuous and dispersed phases to the surface pores of ICCs in a controlled manner. This drove us to develop a new methodology to incorporate the 3D ICC structure into a selective area of a planar microfluidic channel to continuously introduce the dispersed phase through the internal pores and the continuous phase to the surface.

In this study, we propose a new approach to the development of a massively parallelized droplet generation strategy using microfluidic devices, seamlessly implementing ICC structures. A conceptual diagram of the device and the droplet generation mechanism is shown in Fig. 1. In this device, a main channel for introducing a continuous phase and side channels for introducing a dispersed phase are connected with the ICC structure. The surface micropores of the ICC structures, selectively formed on the sidewalls of the main channels, function as parallelized micronozzles for droplet generation. This configuration dramatically improves

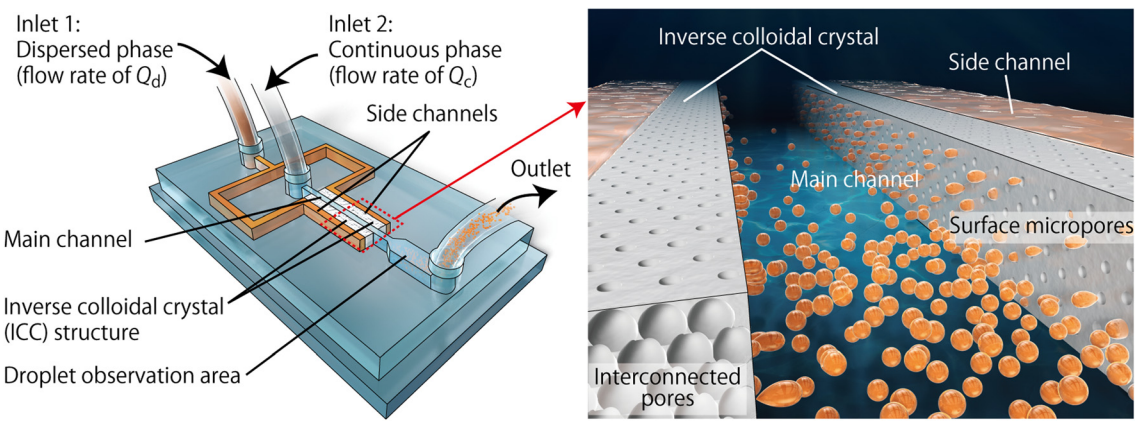

Fig. 1 Schematic image of the microfluidic device incorporating the inverse colloidal crystal (ICC) structure that realizes massively parallel droplet generation through the 2D-arranged surface micropores on the channel wall. The dispersed phase of an aqueous solution and the continuous phase of an oil are introduced from inlets 1 and 2, respectively. The side channels are dead-ended, and connected with the main channel through the ICC structure.

the droplet generation throughput even though only a single planar microchannel structure is used. The bottom and top surfaces of the microchannel are intact PDMS; these are transparent and facilitate the observation of droplet-generation behaviors. To prove this concept, we first developed a new process of creating an all-PDMS microfluidic device with the ICC structures, using spherical non-crosslinked poly(methyl methacrylate) (PMMA) microparticles as the porogen. After characterizing the microdevice and the ICC structures, we performed parallelized droplet generation experiments, attempted to control the size of the droplets, and applied this approach to the production of biopolymer microparticles using polysaccharide (alginate) or protein (collagen) as the material. Moreover, the droplet generation efficiency was further increased by designing and employing a parallelized microchannel system.

Materials and methods

Materials

Olive oil, oleic acid, Span 80, sodium fluorescein, acetone, methyl acetate, ethanol, methanol, calcium chloride dihydrate, acetic acid, and 25% glutaraldehyde solution were obtained from Fujifilm Wako Pure Chemical (Osaka, Japan). Mineral oil was obtained from Nacalai Tesque (Kyoto, Japan). Tetraglycerin monolaurate condensed ricinoleic acid ester (CR-310) was kindly supplied by Sakamoto Yakuhin Kogyo (Osaka, Japan). Polyvinylpyrrolidone (PVP; K = 30) and methyl methacrylate (MMA) were obtained from Kanto Chemical, Tokyo, Japan; MMA was purified by distillation under reduced pressure, and PVP was used as received. Sodium alginate (IL-6G) was obtained from Kimica (Tokyo, Japan). 2-Methyl-1-propanol was obtained from Sigma-Aldrich (MO, USA). Native collagen acidic solution (type I, from bovine dermis, IAC-50, 5 mg mL^{-1}) was obtained from Koken (Tokyo, Japan). Non-crosslinked PMMA microparticles (average φ ± SD of 28.5 ± 2.0 μm, coefficient of variation (CV) of 7.1%) were obtained from Sekisui Kasei (Osaka, Japan). PDMS prepolymer (Silpot 184) was obtained from Dow Corning Toray (Tokyo, Japan). Trimethoxy(1*H*,1*H*,2*H*,2*H*-heptadecafluorodecyl) silane (abbreviated as fluorosilane) and 2,2′-azobis(isobutyronitrile) (AIBN) were obtained from Tokyo Chemical Industry (Tokyo, Japan). All other chemicals were of analytical grade.

Preparation of small-sized sacrificial PMMA particles

The single micrometer-sized PMMA particles were prepared by dispersion polymerization of MMA according to a previous report[54] with modifications. In brief, MMA (60 mmol, 6.0 g), AIBN (750 μmol, 0.123 g), and PVP (600 mg) were dissolved in a mixture of methanol/H_2O (45 g/15 g) and poured into a 200 mL three-necked flask equipped with a paddle stirrer. The flask was purged with N_2 gas for 30 min while stirring at 100 rpm. The system was kept at 70 °C with stirring at 120 rpm. After 6 h, the polymerization reaction was stopped by cooling the system in an ice bath. Aggregates were removed *via* filtration through a 150 μm mesh filter and the PMMA particles obtained were centrifuged at 3000 rpm for 10 min. The resulting PMMA particles were then redispersed in methanol and centrifuged twice at 1000 rpm for 10 min. Finally, after centrifugation at 1000 rpm for 10 min, deionized (DI) water was added to obtain the aqueous dispersion of PMMA. Scanning electron microscopy (SEM; VE-8800, Keyence, Osaka, Japan) was used to observe the obtained particles.

Design and fabrication of the microfluidic device with the inverse colloidal crystal (ICC) structure

The design of the microfluidic device used in this experiment is shown in Fig. 2(a). This device was formed by bonding a lower flat PDMS plate and an upper plate with the microchannel and the ICC structures. Inlet 1 was for introducing the dispersed phase and inlet 2 for introducing

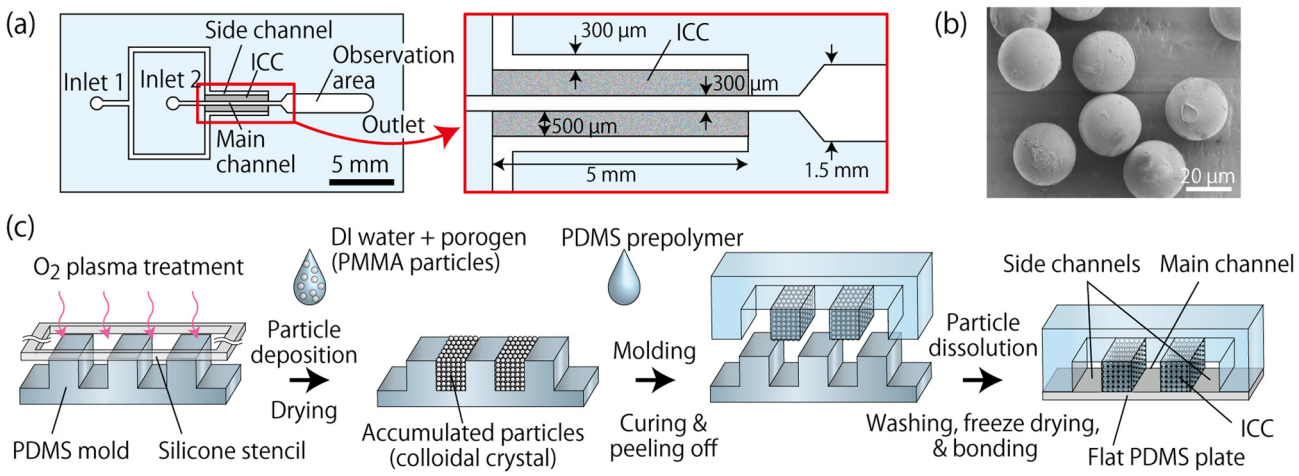

Fig. 2 (a) Design of the microfluidic device with the ICC structure. The depth of the channel was uniformly ~200 μm. (b) SEM image of the PMMA particles (average φ of 28.5 μm) used as the porogen to create the ICC structure. (c) The fabrication process of the microfluidic device composed of the top plate with the channels and ICC and a flat bottom plate.

the continuous phase. The main channel from inlet 2 and the side channels from inlet 1 were indirectly connected by the ICC structure with the size of 0.5 × 5 mm. The area of the main channel near the outlet was broadened to facilitate observation of the generated droplets ("the observation area"). The widths of the main and the side channels were 300 μm, and the channel depth was uniformly ~200 μm.

We used two types of non-crosslinked PMMA particles as the porogen, but larger particles (28.5 ± 2.0 μm; Fig. 2(b)) were mainly used unless otherwise noted. The fabrication process of the microfluidic device is illustrated in Fig. 2(c). First, a master mold was prepared by patterning SU-8 3050 photoresist on a Si wafer through standard soft lithography. Then, a PDMS-based mold was prepared by casting PDMS prepolymer on the master mold and curing, and this process was repeated one more time. The PDMS mold with a convex channel structure was treated with O_2 plasma using a plasma reactor (PR-500; Yamato Scientific, Tokyo, Japan) and then with a 1% fluorosilane solution in methanol. The local area of the fluorosilane-treated secondary mold was further treated with O_2 plasma using a silicone stencil to render the selective region (ICC region) hydrophilic.

Next, a suspension of the PMMA particles in DI water (conc. of ~20% (v/v)) was dropped on the hydrophilized area and the particles were accumulated between the main and the side channel structures. Particles remaining on the main/side channels were removed using adhesive tape. After drying at 40 °C, PDMS prepolymer was cast onto the entire mold and then cured. The cured PDMS plate peeled off from the mold was soaked overnight in acetone to dissolve the embedded PMMA particles. The plate was then washed with acetone, soaked in DI water, and freeze-dried at −90 °C, 20 Pa for 30 min using a vacuum freeze-dryer (FDS-1000; Tokyo Rikakikai, Tokyo, Japan). The obtained PDMS plate with the ICC structure and a flat PDMS plate were treated with O_2 plasma and bonded. The morphology of the pores was observed with SEM, and the pore size was analyzed using Image J software (NIH, Bethesda, MD, USA).

Production of microdroplets

In this study, water-in-oil (W/O) droplets were formed mainly using two types of oils with different viscosities as the continuous phase (olive oil and mineral oil). Deionized (DI) water with 1 mM sodium fluorescein was used as the dispersed phase, unless otherwise noted. To ensure the droplet stability, CR-310 (5% (w/w)) and Span 80 (1% (w/w)) were added to olive oil and mineral oil, respectively. The viscosities of these continuous phases at room temperature, measured by using a vibration-type viscometer (VM-10A, Sekonic, Tokyo, Japan), were 73.3 and 18.0 mPa s, respectively. The continuous/dispersed phases were continuously pumped into the device using syringe pumps (KDS200, KD Scientific, MA, USA). The generation behaviors of droplets were observed using an inverted optical/fluorescence microscope (IX-81, Olympus, Tokyo, Japan) with a CCD camera (DP74, Olympus). The size of the droplets was measured from the microscopic images.

Production of alginate microparticles

A 0.5% sodium alginate (Na-alg) solution in DI water was used as the dispersed phase and olive oil with 5% (w/w) of CR-310 was used as the continuous phase. Calcified oil[55,56] was used for the gelation of the formed droplets of Na-alg outside the channel; the calcified oil was prepared first by dissolving 10% (w/v) $CaCl_2$ in 2-methyl-1-propanol by ultrasonication and then this solution was added into oleic acid at a ratio of 10% (v/v). The generated droplets of Na-alg were introduced through a PTFE tube into the stirred calcified oil for gelation. The subsequently generated calcium alginate (Ca-alg) particles were washed three times with 99.5% ethanol *via* centrifugation, then introduced into an aqueous solution of 0.1 M $CaCl_2$ and observed under the optical microscope. In addition, the particle morphology was observed by SEM, after washing the particles with DI water, lyophilized, and sputter-coated by a thin Au layer.

Production of crosslinked collagen microparticles

We employed a previously developed technique of forming microparticles by solvent extraction using water-soluble organic solvents.[30] An aqueous solution of 0.1% type I collagen in 20 mM acetic acid was used as the dispersed phase and olive oil with 5% (w/w) CR-310 was used as the continuous phase. The droplets produced were introduced into a stirred vial with methyl acetate through a thin tube attached to the outlet of the channel. Aqueous solution of glutaraldehyde was then added to this solution at a final concentration of 2.5% and the dehydrated collagen particles were crosslinked for 90 min at room temperature. PBS was then added, and the aqueous phase with the particles was collected and washed twice with ethanol by centrifugation to remove excess oil phase. Finally, the particles were dispersed in DI water and their morphology was observed by optical microscopy.

Results and discussions

Fabrication and characterization of the ICC structure

In order to produce micrometer-sized droplets by the presented ICC-based approach, the first requirement is to ensure the uniformity in the size and shape of the surface pores of the ICC structure. To date, several methods for the fabrication of sponge-like PDMS materials have been reported,[44] including a method using spherical polystyrene particles as porogen.[53] However, to the best of our knowledge, integration of ICCs having circular and uniformly sized surfaces with a microfluidic channel has not been reported. Therefore, we propose a new approach to the formation of circular micropores on the surface (sidewall) of the microchannel. Sacrificial PMMA microparticles as porogen with a relatively small variance in diameter (CV of

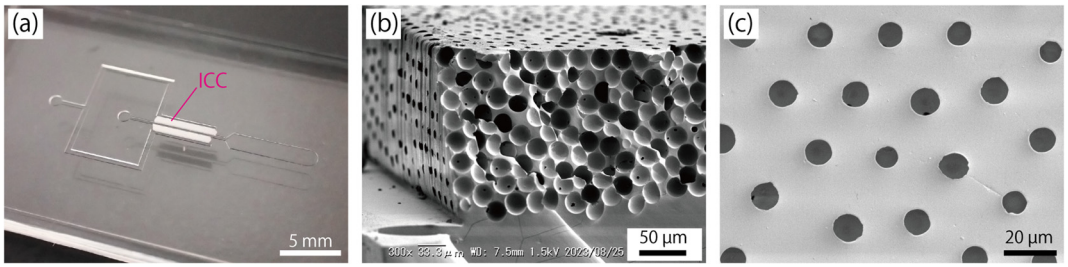

Fig. 3 (a) Photograph of the ICC-incorporated PDMS plate with the channel structure before bonding with a flat PDMS plate. (b and c) SEM images showing (b) the cross section of the ICC structure and (c) the surface pores on the ICC. ICC was created using PMMA microparticles (average φ of 28.5 μm) as the porogen.

7.1%) were deposited on a selective region of a mold for the microfluidic channel. Because the porogen particles used in this study were not chemically crosslinked, they were easily dissolvable in a polar organic solvent (acetone), which is compatible with PDMS.

A photograph of the fabricated PDMS plate with the ICCs is shown in Fig. 3(a); the ICC area was whitish and opaque, while the rest of the device was transparent. By applying O_2 plasma treatment only to the particle deposition area in advance, spreading of the particle suspension was suppressed and the particles could be selectively accumulated between the channel structures. Particles remaining on the channel structure of the mold were easily removed using adhesive tape, facilitating the observation of the droplet formation in the main channel. After dissolving the porogen and freeze-drying, the surface of the ICC structure was flattened.

SEM images of the cross section and the surface of the ICC structure are shown in Fig. 3(b and c). From the surface observation, circular micropores with diameters of 10.3 ± 1.2 μm (CV of 11.4%) were formed. These micropores were mostly hexagonally arranged, suggesting that the sacrificial porogens were densely packed at the deposition process. The density of these surface pores was 1.3×10^3 pores per mm^2 (the area ratio of the surface pore of 10.9%), indicating that a total of ~2.6×10^3 micropores were formed on both sidewalls of the main channel. It was naturally anticipated that the use of more uniformly sized porogens would result in the formation of micropores with a smaller size distribution. The SEM image of the cross section revealed that smaller connecting pores were observed between the spherical voids, suggesting that the internal pores were interconnected. The upper surface of the ICC structure was smooth and flat, enabling the O_2 plasma-based seamless bonding of the ICC surface with a flat PDMS plate.

Droplet generation using the microdevice

The presented microfluidic device was made entirely and solely of PDMS, which is hydrophobic and suitable for the formation of W/O droplets. In the following droplet generation experiments, we first used olive oil as the continuous phase and generated aqueous droplets of sodium fluorescein solution. Fig. 4 and Movie S1† show microscopic images and a movie of the microdroplets being formed in the main channel and flowing through the observation area. The dispersed phase of the aqueous solution, introduced from inlet 1, flowed through the ICC structure, and was extruded from the surface pores. As in the case of droplet generation schemes using through holes,[43] it was expected that the thin thread extended from the being formed droplet is torn by the viscoelastic shear force exerted from the continuous phase, and the torn thread of the dispersed phase is absorbed into the dispersed phase inside the pore, forming a droplet. Consequently, a tremendous number of droplets were formed from the densely arranged micropores on the microchannel walls. The number of droplets increased when the flow rate of the dispersed phase (Q_d) was increased, whereas that of the continuous phase (Q_c) was fixed at 100 μL min^{-1}. The sizes of the droplets generated were 30.5 ± 4.1 μm (CV: 13.5%) and 36.4 ± 6.1 μm (CV: 16.6%) when the Q_d values were 10 μL min^{-1} and 50 μL min^{-1}, respectively, and the droplet sizes were relatively uniform. Even though the Q_d was increased 5-fold, the droplet diameter showed only a ~1.2-fold increase; this would be because the shear force applied to the droplets that were being formed from the viscous continuous phase was not significantly changed. That is, when Q_d was increased, the number of the micropores on the channel walls, which functioned as active nozzles for droplet formation, was increased. Additionally, for the relatively small Q_d value conditions, fewer droplets were formed near the upstream area in the main channel. This may be due to the balance between the applied pressure to the main/side channels and the hydrodynamic resistance of the ICC.

Under these conditions, the speed of droplet production was estimated to be 1.1×10^4 and 3.3×10^4 droplets per s for the Q_d conditions of 10 and 50 μL min^{-1}, respectively. In previous studies in which droplets with similar sizes were produced using a T-shaped channel[17] and a flow-focusing channel,[57] several hundreds of droplets were produced per second. In marked contrast, the device presented here achieved a dramatic improvement of the droplet generation throughput even when employing a simple planar microchannel structure. The production speed of our device was almost comparable to that of parallelized microchannels; for example, ~1×10^5 droplets per s was reported using a

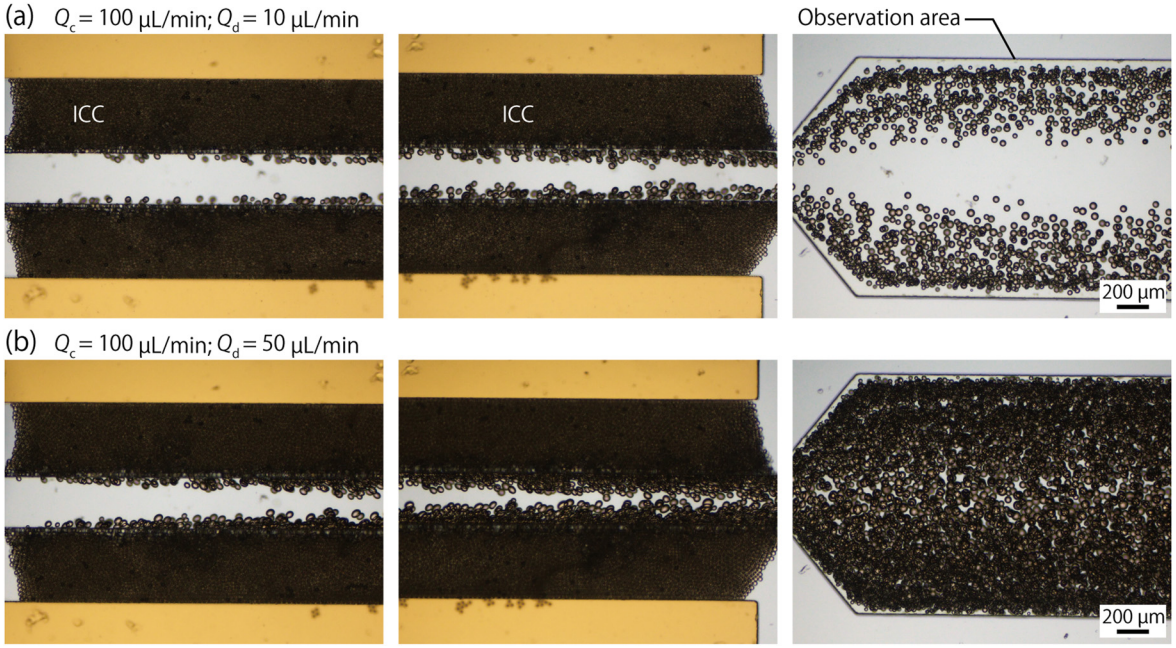

Fig. 4 Optical microscopic images showing the formation behaviors of microdroplets using the presented microfluidic device. Q_d was (a) 10 μL min^{-1} and (b) 50 μL min^{-1}, whereas Q_c was constant at 100 μL min^{-1}. Olive oil and an aqueous solution of sodium fluorescein were used as the continuous and dispersed phases, respectively. The left, middle, and right panels show the main channels near the entrance of the ICC, exit of the ICC, and the droplet observation area, respectively.

device with 144 parallelized channels.[36] The presented approach is advantageous because it completely dispenses with the large-scale fabrication process, owing to the integrated 3D ICC structure with the 2D channels that functioned as massively parallel micropores for droplet generation. The CV value of the droplet diameter obtained by the presented approach was larger than 10%, which was slightly higher than the CV values (typically 3–10%) obtained in previous studies using single microchannels. Since the variation of droplet diameter corresponded to that of the pore size of the ICC surface, it is considered that more uniformly sized droplets can be formed when much more monodispersed porogens were used. Furthermore, it is worth noting that satellite droplets were formed and droplet size uniformity was compromised when Q_c exceeded ~200 μL min^{-1} for olive oil. It would be necessary to set an upper limit for the flow rate depending on the type of the continuous phase used.

Effects of continuous phase on droplet size

Next, two types of oils (olive oil and mineral oil) with different viscosities and interfacial tensions were tested as the continuous phase to investigate the viscosity effect on droplet formation and control the droplet size. Fig. 5(a) and (b) show microscopic images of fluorescent droplets collected from the device using olive oil or mineral oil as the continuous phase. We confirmed that these droplets were stable outside of the microchannel. Fig. 5(c) shows the droplet size when Q_c was varied from 10 to 100 μL min^{-1} whereas the ratio of Q_c and Q_d was fixed at 10 : 1. From this result, it is clear that the droplet size decreased with the increase in the flow rate. When Q_c was 100 μL min^{-1} for olive oil, droplets as small as ~30 μm were obtained. The effect of the viscosity of the continuous phase was also revealed; droplets produced using mineral oil with a lower viscosity (18.0 mPa s) were larger than those produced using olive oil (73.3 mPa s) as the continuous phase. Additionally, there should be an influence of the interfacial tension on the droplet size. The interfacial tensions between the continuous and dispersed phases were measured using a tensiometer (CBVP-Z, Kyowa Interfacial Science, Saitama, Japan), and the values were 2.9 mN m^{-1} for olive oil with CR-310 and 5.0 mN m^{-1} for mineral oil with Span 80, respectively. These results suggested that the increased shear force on the droplets and the decreased interfacial tension resulted in the formation of smaller droplets. Compared to other techniques for droplet generation, such as conventional membrane emulsification techniques, where the dynamic control of droplet size is difficult, the presented system is advantageous because the droplet size can be tuned by adjusting the applied shear force.

Preparation of alginate microparticles

As applications of the presented droplet generation system, we first produced polysaccharide microparticles. Alginate was used as the material; alginate can be rapidly gelled in the presence of multivalent cations such as Ca^{2+} and Ba^{2+} ions.[58] Alginate-based microparticles are often used as carriers for

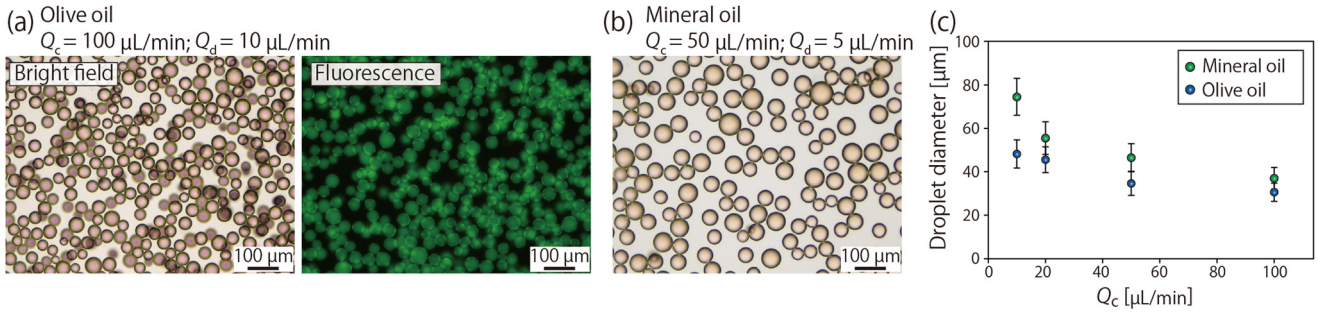

Fig. 5 (a and b) Bright field and fluorescence micrographs showing the droplets collected from the outlet of the device. Droplets of an aqueous solution of sodium fluorescein were formed using (a) olive oil and (b) mineral oil as the continuous phase, respectively. (c) Relationship between Q_c and the droplet diameter, when two types of oils with different viscosities were used as the continuous phase. The ratio of Q_c and Q_d was kept constant at 10 : 1. Each data point is the mean ± SD of ~300 droplets.

drug delivery[59] and scaffold materials for cell culture.[60,61] The scheme for producing Ca-alg particles is shown in Fig. 6(a); aqueous droplets of Na-alg were generated using olive oil as the continuous phase, and calcified oil was used to turn the generated Na-alg droplets into Ca-alg particles. Fig. 6(b) shows a microscopic image of the Na-alg droplets formed in the microchannel and flowing through the observation area. When Q_c and Q_d were 100 and 10 μL min^{-1}, respectively, the average diameter ± SD of the droplets was 35.8 ± 5.0 μm (CV of 13.8%). Compared to the result shown in Fig. 5(c), where the average droplet diameter was 30.6 μm under the same flow rate condition, the droplet diameter was slightly increased. This would be due to the increased viscosity of the Na-alg solution (8.9 mPa s) compared to that of water (0.9 mPa s). Fig. 6(c) and (d) show an optical micrograph of the obtained Ca-alg hydrogel particles in an aqueous solution and an SEM image of the lyophilized particles, respectively. The particles are spherical in morphology, which can be attributed to the rapid and uniform gelation of the droplets. The average particle diameter ± SD measured from the optical microscope images was 8.2 ± 1.5 μm (CV of 17.9%). The small size of the obtained Ca-alg particles compared to the droplets may have been due to the volume contraction of the aqueous Na-alg solution during gelation.[62] This result indicated that the presented microdevice is capable of efficiently producing Ca-alg particles of single micrometer sized in a high throughput manner.

Preparation of collagen microparticles

Next, we attempted to produce collagen microparticles. Collagen is the main protein component of the extracellular matrix and is frequently used as a scaffold for mammalian cell culture owing to its cell-supportive characteristics. Collagen particles of similar size to cells have been reported to regulate the cell density and upregulate cell functions and viability in 3D cell culture systems.[30,63] In this experiment, aqueous droplets of type I collagen were formed in the microdevice, which were subsequently dehydrated with methyl acetate, a water-soluble organic solvent, and then the collagen molecules were crosslinked with glutaraldehyde. The viscosity of the 0.1% collagen solution was measured as 3.8 mPa s.

Fig. 7(a) shows the droplets flowing in the channel generated when olive oil was used as the continuous phase (Q_c: 100 μL min^{-1}; Q_d: 50 μL min^{-1}). The average diameter ± SD of the generated droplets at the beginning of the experiment was 41.5 ± 7.9 μm. This value was comparable to but slightly (~15%) larger than the droplet diameter of the fluorescein solution shown in Fig. 4(b); as in the case of the Na-alg droplets, the increased viscosity of the dispersed phase resulted in the formation of larger droplets. In this experiment, we introduced an aqueous solution of protein that is considered to adhere to the surface, but there was no significant change in the size of the droplets after a relatively long time of operation; the average diameter ± SD of the droplets was 42.1 ± 8.4 μm after one hour of experimental manipulation. The formed collagen microparticles after

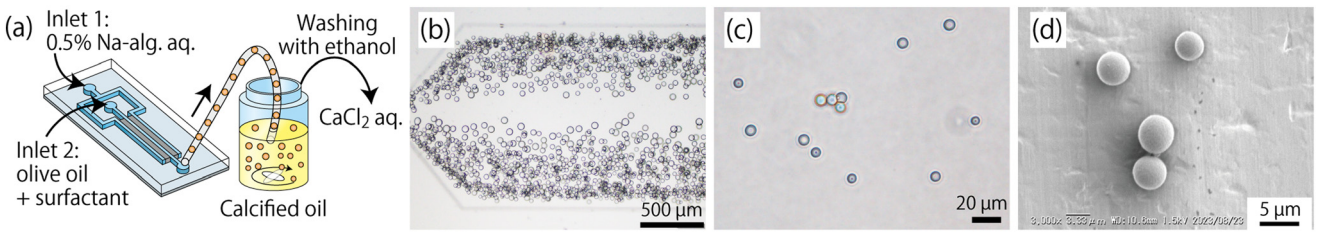

Fig. 6 Production of Ca-alginate (Ca-alg) microparticles. (a) Schematic image showing the production process of the Ca-alg particles. (b) Microscopic image showing the droplets of Na-alg. Solution in the observation area. (c) Micrograph showing the obtained Ca-alg particles suspended in a $CaCl_2$ solution. (d) SEM image of the dried Ca-alg microparticles.

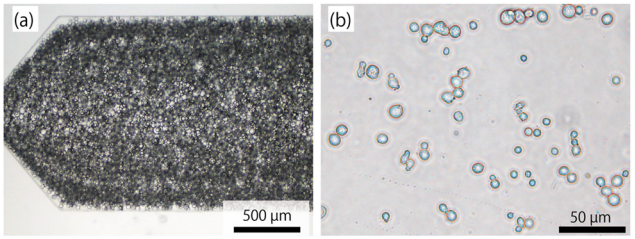

Fig. 7 (a) Droplets of collagen solution flowing through the observation area. Q_c and Q_d were 100 and 50 μL min^{-1}, respectively. (b) Optical micrograph showing the obtained collagen microparticles.

droplet dehydration, collagen concentration, and chemical crosslinking are shown in Fig. 7(b). The obtained particles exhibited relatively spherical morphology, but some of the particles were aggregated. The average diameter ± SD of the particles was 7.0 ± 1.4 μm, with a relatively large size distribution (CV of 20.6%) compared to the Ca-alg particles shown in Fig. 6. We assumed that fusion of condensed collagen droplets and/or particles occurred during the relatively long crosslinking process, resulting in the variations in particle size and morphology. The number of particles produced was ~150 times higher than that of a previous study using a single microfluidic channel to produce collagen particles of similar size (150 droplets per s) and comparable to that of membrane emulsification (~10 000 droplet per s, CV of ~30%).[30] From this result and the results of alginate particle production, we have successfully confirmed the high capability of the presented system to produce microparticles composed of natural biopolymers, including polysaccharides and proteins. The high particle productivity and the controllability in particle size of the device will expand the range of applications of biopolymer particles in biomedical research, drug development, and tissue engineering.

Droplet generation using ICCs with smaller micropores

Although we have demonstrated the controllability of droplet size through the tuning of the flow rates and the viscosity of the continuous phase (Fig. 5(c)), it could be naturally anticipated that droplets with significantly different sizes would be generated if ICCs with much larger/smaller pores were employed. To verify this concept, we next attempted to prepare an ICC structure with smaller pores. Non-crosslinked PMMA particles with an average diameter ± SD of 6.2 ± 0.4 μm (CV of 6.8%) were synthesized by dispersion polymerization (Fig. 8(a)) and used as the porogen. For this experiment, a microdevice with a smaller main/side channel width of 200 μm and a channel depth of 50 μm was fabricated and used.

An SEM image of the surface pores of the ICC prepared using the smaller porogen is shown in Fig. 8(b). As with the larger particles, circular micropores were formed and were densely arranged, but the pore size was smaller (3.5 ± 0.3 μm, CV of 9.9%) than that shown in Fig. 3(c). The micropore density was 2.3 × 10^4 pores per mm^2, ~18 times higher than that of the pores prepared with the larger particles. The area ratio of the surface pore was 22.6%. Fig. 8(c) shows the microscopic image of droplets formed using olive oil as the continuous phase and flowing in the observation area, with Q_c and Q_d of 100 and 10 μL min^{-1}, respectively. Droplets were mainly generated near the downstream area of the main channel, as was the case when the relative Q_d was small for the ICC devices with large pores. The average droplet diameter ± SD was 8.8 ± 1.3 μm, which was ~29% of that of droplets produced by larger pores under the same flow rate conditions. Since the surface pore size was ~34%, it was clarified that the droplet diameter and the pore size were almost in a proportional relationship. The droplet formation speed was 3.7 × 10^4 droplets per s, also showing the high speed of droplet generation. These results clarified that the size of the micropores on the ICC surface could be changed by using porogens with different sizes, which is a rational strategy to widely control the droplet size. Although not tested, it was expected that the use of much larger porogens would result in the formation of larger pores and thus larger droplets.

Further increase of the throughput by parallelization concept

Although the microfluidics experiments described in the above sections were performed using a single channel system, it would be meaningful to attempt to further increase the droplet generation throughput by parallelization, as described in many previous works. To characterize the scalability of the presented system, we designed and fabricated a microfluidic device with eight parallel unit structures as a proof-of-concept trial. The design and a photograph of the two-layer microfluidic device, composed of two plates with the channels

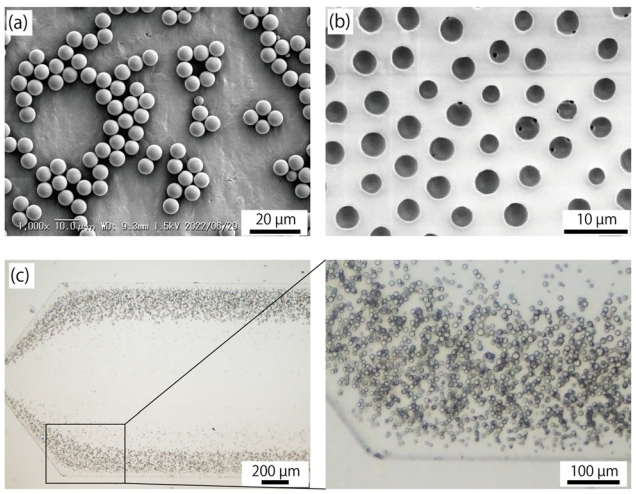

Fig. 8 (a) SEM images of non-crosslinked PMMA particles with the average diameter ± SD of 6.2 ± 0.4 μm. (b) SEM image of the micropores on the ICC surface prepared using the small porogens shown in (a). The average diameter ± SD was 3.5 ± 0.3 μm. (c) Microdroplets generated from the ICC and flowing in the observation area. Olive oil was used as the continuous phase. Q_c and Q_d were 100 and 10 μL min^{-1}, respectively. The droplet diameter was 8.8 ± 1.3 μm.

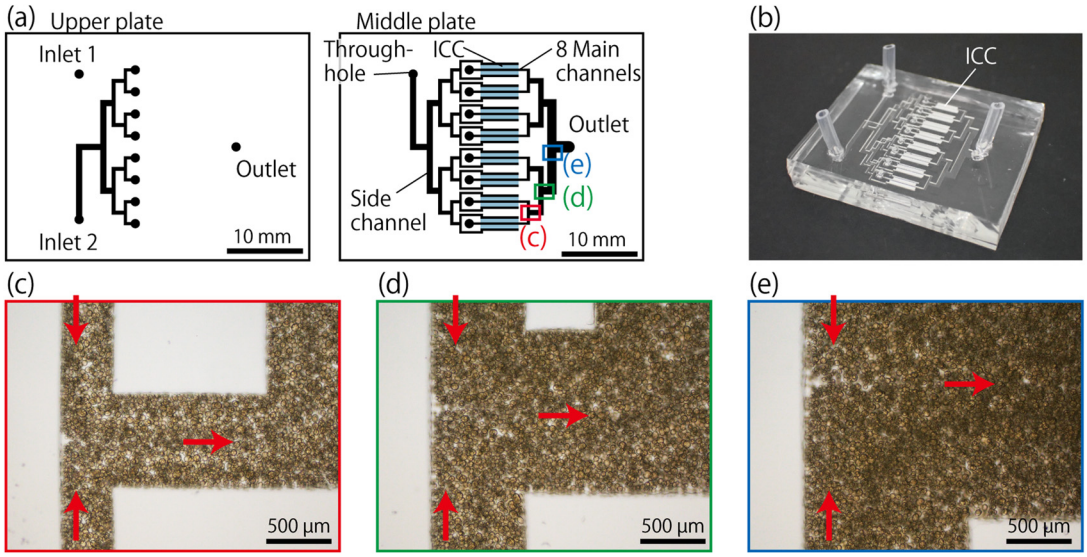

Fig. 9 (a) Design of the two-layer microfluidic device with 8 parallel channels for high-throughput droplet production. (b) Photograph of the fabricated device. (c–e) Micrographs showing generated droplets flowing through the outlet channel at different positions; these panels correspond to those indicated in (a), respectively. Red arrows indicate the direction of the flow. Q_c and Q_d were 800 and 400 μL min^{-1}, respectively. The average droplet diameter ± SD was 33.1 μm ± 3.6 μm, with total production speed of 1.5 × 10^5 droplets per s.

and/or ICCs and one flat plate, are shown in Fig. 9(a) and (b), respectively. In the fabrication process of this device, a silicone stencil with a large rectangular hole was used to simultaneously make the 16 parallelized ICC regions of the mold hydrophilic.

Fig. 9(c–e) show the microscopic images of the droplets generated from the ICCs and flowing through the outlet junctions of the microchannel. Olive oil was used as the continuous phase with Q_c and Q_d of 800 and 400 μL min^{-1}, respectively. The main channel network was designed to have gradually wider outlet junctions to reduce the fluid resistance of the outlet channel. We confirmed that relatively uniform-sized microdroplets were formed with the similar droplet size and variation as in the single-microchannel experiment with Q_c and Q_d of 100 and 50 μL min^{-1}, respectively. Observations of the locations of the merging flows at each junction suggested that the flow rates through the eight parallel channels were almost equal. This may be due, at least partially, to the relatively uniform hydrodynamic resistances of the parallel ICC regions. These results suggest that the presented system is highly scalable and flexible in microchannel design. It would be possible to further optimize the parameters of the microfluidic device depending on the viscosity of the fluid, including the shape of the microchannel and the configuration of the ICC, to reduce the overall pressure while ensuring sufficient throughput of droplet generation.

Conclusions

We have proposed an ultra-high throughput droplet formation strategy using parallelized micropores formed on the microchannel walls. The most important key to the successful upgrading of the microfluidic droplet generation is the seamless integration of the 3D ICC structure into a conventional planar microfluidic channel. For this purpose, a bottom-up fabrication strategy *via* selective accumulation and dissolution of sacrificial porogens was newly developed. We have shown that circular micropores on the surface of the ICC functioned as densely parallelized nozzles for the mass production of droplets. Despite the simple design of the microchannel structure, the proposed system enables droplet formation throughput 100–1000 times higher than conventional microdevices for droplet preparation.

In the experiment, droplet formation was first performed using two types of continuous phases with different viscosities as a model, and then two types of biopolymer particles were prepared using droplets as templates. Micrometer-sized particles made of polysaccharide- or protein-based materials would be valuable in various research/medical applications, including scaffolds for tissue engineering, DDS carriers, and general biological studies. Aside from particle preparation, droplets produced using the presented microfluidic system can be employed as reactors for digital assays with single molecule/cell incorporation or for the construction of functional liquid–liquid dispersion systems (*e.g.*, double emulsions) with dramatically increased speed and efficiency of droplet formation potential.

Conflicts of interest

There are no conflicts to declare.

Acknowledgements

This study was supported in part by Grants-in-Aid for Scientific Research (22H01875 and 22K18311) from the

Ministry of Education, Culture, Sports, Science, and Technology of Japan. We thank Mr. Shun Yamazaki at Chiba University for technical assistance.

References

1 A. Forigua, R. L. Kirsch, S. M. Willerth and K. S. Elvira, *J. Controlled Release*, 2021, **333**, 258–268.
2 M. Duran, A. Serrano, A. Nikulin, J. L. Dauvergne, L. Derzsi and E. Palomo del Barrio, *Mater. Des.*, 2022, **223**, 111230.
3 Y. Ding, P. D. Howes and A. J. deMello, *Anal. Chem.*, 2020, **92**, 132–149.
4 W. Zheng, S. Zhao, Y. Yin, H. Zhang, D. M. Needham, E. D. Evans, C. L. Dai, P. J. Lu, E. J. Alm and D. A. Weitz, *Science*, 2022, **376**, eabm1483.
5 L. Zhang, P. Rokshana, Y. Yu, Y. Zhao and F. Ye, *Small*, 2022, **18**, e2107858.
6 M. Mizuno, T. Toyota, M. Konishi, Y. Kageyama, M. Yamada and M. Seki, *Langmuir*, 2015, **31**, 2334–2341.
7 G. Zhang and J. M. Sun, *Int. J. Nanomed.*, 2021, **16**, 7391–7416.
8 S. H. Jung, S. Bulut, L. P. B. Busca Guerzoni, D. Gunther, S. Braun, L. De Laporte and A. Pich, *J. Colloid Interface Sci.*, 2022, **617**, 409–421.
9 D. Dendukuri, K. Tsoi, T. A. Hatton and P. S. Doyle, *Langmuir*, 2005, **21**, 2113–2116.
10 A. Miyama, M. Yamada, S. Sugaya and M. Seki, *RSC Adv.*, 2013, **3**, 12299.
11 Y. Tian and E. A. Lipke, *ACS Biomater. Sci. Eng.*, 2020, **6**, 6435–6444.
12 C. Yang, Y. Yu, Y. Zhao and L. Shang, *Research*, 2023, **6**, 0034.
13 J. F. Edd, D. Di Carlo, K. J. Humphry, S. Koster, D. Irimia, D. A. Weitz and M. Toner, *Lab Chip*, 2008, **8**, 1262–1264.
14 L. M. Caballero Aguilar, S. Duchi, C. Onofrillo, C. D. O'Connell, C. Di Bella and S. E. Moulton, *J. Colloid Interface Sci.*, 2021, **587**, 240–251.
15 S. Sugiura, M. Nakajima, T. Oda, M. Satake and M. Seki, *J. Colloid Interface Sci.*, 2004, **269**, 178–185.
16 J. Yao, F. Lin, H. S. Kim and J. Park, *Micromachines*, 2019, **10**, 808.
17 M. Yamada, S. Doi, H. Maenaka, M. Yasuda and M. Seki, *J. Colloid Interface Sci.*, 2008, **321**, 401–407.
18 M. L. J. Steegmans, K. G. P. H. Schroen and R. M. Boom, *Langmuir*, 2009, **25**, 3396–3401.
19 P. He, D. Barthès-Biesel and E. Leclerc, *Microfluid. Nanofluid.*, 2009, **9**, 293–301.
20 A. Lashkaripour, C. Rodriguez, L. Ortiz and D. Densmore, *Lab Chip*, 2019, **19**, 1041–1053.
21 A. M. Ibrahim, J. I. Padovani, R. T. Howe and Y. H. Anis, *Micromachines*, 2021, **12**, 590.
22 Z. Li, A. M. Leshansky, L. M. Pismen and P. Tabeling, *Lab Chip*, 2015, **15**, 1023–1031.
23 I. Chakraborty, J. Ricouvier, P. Yazhgur, P. Tabeling and A. M. Leshansky, *Lab Chip*, 2017, **17**, 3609–3620.
24 A. S. Utada, L. Y. Chu, A. Fernandez-Nieves, D. R. Link, C. Holtze and D. A. Weitz, *MRS Bull.*, 2007, **32**, 702–708.
25 E. E. Ekanem, Z. Zhang and G. T. Vladisavljevic, *J. Colloid Interface Sci.*, 2017, **498**, 387–394.
26 B. Haney, D. Chen, L. H. Cai, D. Weitz and S. Ramakrishnan, *Langmuir*, 2019, **35**, 4693–4701.
27 S. Y. Teh, R. Lin, L. H. Hung and A. P. Lee, *Lab Chip*, 2008, **8**, 198–220.
28 N. Tarchichi, F. Chollet and J. F. Manceau, *Microfluid. Nanofluid.*, 2012, **14**, 45–51.
29 M. Costantini, C. Colosi, J. Guzowski, A. Barbetta, J. Jaroszewicz, W. Swieszkowski, M. Dentini and P. Garstecki, *J. Mater. Chem. B*, 2014, **2**, 2290–2300.
30 M. Yamada, A. Hori, S. Sugaya, Y. Yajima, R. Utoh, M. Yamato and M. Seki, *Lab Chip*, 2015, **15**, 3941–3951.
31 C. T. Riche, E. J. Roberts, M. Gupta, R. L. Brutchey and N. Malmstadt, *Nat. Commun.*, 2016, **7**, 10780.
32 E. Castro-Hernández, P. García-Sánchez, A. Velencoso-Gómez, A. Silas-Jurado, D. F. Rivas and A. Ramos, *Microfluid. Nanofluid.*, 2017, **21**, 158.
33 P. Zhu and L. Wang, *Lab Chip*, 2016, **17**, 34–75.
34 H.-H. Jeong, D. Issadore and D. Lee, *Korean J. Chem. Eng.*, 2016, **33**, 1757–1766.
35 L. Jiang, H. Yang, W. Cheng, Z. Ni and N. Xiang, *Analyst*, 2023, **148**, 203–221.
36 T. Nisisako, T. Ando and T. Hatsuzawa, *Lab Chip*, 2012, **12**, 3426–3435.
37 M. B. Romanowsky, A. R. Abate, A. Rotem, C. Holtze and D. A. Weitz, *Lab Chip*, 2012, **12**, 802–807.
38 H. H. Kim, Y. Cho, D. Baek, K. H. Rho, S. H. Park and S. Lee, *Small*, 2022, **18**, e2205001.
39 H. H. Jeong, V. R. Yelleswarapu, S. Yadavali, D. Issadore and D. Lee, *Lab Chip*, 2015, **15**, 4387–4392.
40 G. T. Vladisavljević, E. E. Ekanem, Z. Zhang, N. Khalid, I. Kobayashi and M. Nakajima, *Chem. Eng. J.*, 2018, **333**, 380–391.
41 Y. Zheng, H. Chen, X. Lin, M. Li, Y. Zhao and L. Shang, *Small*, 2023, **19**, e2206007.
42 C. F. Deng, Y. Y. Su, S. H. Yang, Q. R. Jiang, R. Xie, X. J. Ju, Z. Liu, D. W. Pan, W. Wang and L. Y. Chu, *Lab Chip*, 2022, **22**, 4962–4973.
43 I. Kobayashi, S. Mukataka and M. Nakajima, *J. Colloid Interface Sci.*, 2004, **279**, 277–280.
44 D. Y. Zhu, S. Handschuh-Wang and X. C. Zhou, *J. Mater. Chem. A*, 2017, **5**, 16467–16497.
45 K. Takeuchi, N. Takama, R. Kinoshita, T. Okitsu and B. Kim, *Biomed. Microdevices*, 2020, **22**, 79.
46 M. Takagi, M. Yamada, R. Utoh and M. Seki, *Lab Chip*, 2023, **23**, 2257–2267.
47 S. Liang, Y. Li, J. Yang, J. Zhang, C. He, Y. Liu and X. Zhou, *Adv. Mater. Technol.*, 2016, **1**, 1600117.
48 X. Zhao, L. X. Li, B. C. Li, J. P. Zhang and A. Q. Wang, *J. Mater. Chem. A*, 2014, **2**, 18281–18287.
49 D. H. Kim, M. C. Jung, S. H. Cho, S. H. Kim, H. Y. Kim, H. J. Lee, K. H. Oh and M. W. Moon, *Sci. Rep.*, 2015, **5**, 12908.
50 Q. Zhang, H. Lu, N. Kawazoe and G. Chen, *Acta Biomater.*, 2014, **10**, 2005–2013.

51 L. Wang, Z. Chu, X. Ning, Z. Huang, W. Tang, W. Jiang, J. Ye and C. Chen, *Crystals*, 2022, **12**, 378.
52 B. Yu, S. B. Guo, X. X. Han, Y. Q. Shen and H. L. Cong, *Ferroelectrics*, 2022, **593**, 93–102.
53 S. Kang, J. Lee, S. Lee, S. Kim, J.-K. Kim, H. Algadi, S. Al-Sayari, D.-E. Kim, D. Kim and T. Lee, *Adv. Electron. Mater.*, 2016, **2**, 1600356.
54 T. Taniguchi, T. Ogawa, Y. Kamata, S. Kobaru, N. Takeuchi, M. Kohri, T. Nakahira and T. Wakiya, *Colloids Surf., A*, 2010, **356**, 169–175.
55 D. H. Lee, W. Lee, E. Um and J. K. Park, *Biomicrofluidics*, 2011, **5**, 34117–341179.
56 C. Kim, J. Park and J. Y. Kang, *Biomicrofluidics*, 2014, **8**, 066504.
57 S. Sugaya, M. Yamada, A. Hori and M. Seki, *Biomicrofluidics*, 2013, **7**, 054120.
58 M. Yamada and M. Seki, *J. Chem. Eng. Jpn.*, 2018, **51**, 318–330.
59 D. R. Telange, R. R. Pandharinath, A. M. Pethe, S. P. Jain and P. L. Pingale, *AAPS PharmSciTech*, 2022, **23**, 99.
60 Y. Morimoto, M. Onuki and S. Takeuchi, *Adv. Healthcare Mater.*, 2017, **6**, 1601375.
61 S. Daradmare, H. Son and C. S. Lee, *Langmuir*, 2023, **39**, 13876–13889.
62 Y. Yajima, M. Yamada, E. Yamada, M. Iwase and M. Seki, *Biomicrofluidics*, 2014, **8**, 024115.
63 Y. Yajima, M. Yamada, R. Utoh and M. Seki, *ACS Biomater. Sci. Eng.*, 2017, **3**, 2144–2154.